Journal of Solar Energy Research (JSER)

Journal homepage: www.jser.ut.ac.ir

Boosting Sustainable Dye-Sensitized Solar Cells (DSSCs) Performance via Copper-Doped Manganese Sulfide Nanoparticles: A Comparative Study

Ahmed Nsaif Jasim

Department of Physics, College of Science, University of Diyala, 32001 Baqubah, Diyala, Iraq

ARTICLE INFO

Article Type:

Research Article

Received:2025.10.29
Accepted in revised form:2026.02.20

Keywords:
Cu-doped MnS nanoparticles; co-precipitation method; XRD; sustainable Dye-Sensitized Solar Cells; Optical properties analysis

A B S T R A C T

This study demonstrates a significant enhancement in the performance of sustainable dye-sensitized solar cells (DSSCs) through the integration of copper-doped manganese sulfide (MnS:Cu) nanoparticles as photoanodes. Undoped, 1% Cu, and 3% Cu-doped MnS nanoparticles were synthesized via a facile co-precipitation method. X-ray diffraction confirmed a nano-crystalline structure, with the crystallite size on the (200) plane increasing from 12.60 nm (undoped) to 14.37 nm (3% Cu). Critically, copper doping induced a reduction in the optical band gap from 3.4 eV to 3.2 eV, enhancing light harvesting. Morphological analysis revealed a transformation from large, flat islands (undoped) to a uniform layer of smaller, spherical nano-grains (~43 nm for 3% Cu), which improved dye loading and light scattering. Consequently, the power conversion efficiency of the fabricated DSSCs increased substantially with doping concentration, yielding 0.455%, 0.624%, and 0.905% for undoped, 1% Cu, and 3% Cu-doped MnS-based cells, respectively, under standard illumination (100 mW cm^{-2}, AM 1.5G). This work establishes Cu-doping as a highly effective strategy for tailoring the properties of MnS nanoparticles for efficient solar energy conversion.

1. Introduction

The fascinating combination of semiconductivity and magnetism observed in diluted magnetic semiconductors (DMS) has drawn more attention from researchers [1]. In DMS, the localized magnetic moments significantly interact with the band electrons and holes to produce a range of intriguing phenomena [2]. It has a large optical bandgap of (E_g = 3.1-3.7 eV) and potential use in solar cells, sensors, and photoconductors [3]. MnS is a DMS substance. It is discovered that MnS nanoparticles have p-type semiconducting properties

*Corresponding Author Email: ahmedphy@uodiyala.edu.iq

Cite this article: Jasim, A. Nsaif (2026). Boosting Sustainable Dye-Sensitized Solar Cells (DSSCs) Performance via Copper-Doped Manganese Sulfide Nanoparticles: A Comparative Study. Journal of Solar Energy Research, 11(1), 2891-2902. doi: 10.22059/jser.2026.405234.1663

DOI: 10.22059/jser.2026.405234.1663

[4]. MnS nanoparticles or powders may adopt various polymorphic forms, the most prevalent of which is the rock-salt structure (-MnS), which crystallizes into the zinc-blende or wurtzite structure via low-temperature growth procedures [5]. It has been discovered that between (373 and 673) K, and -MnS can irreversibly convert into the stable -MnS [6]. Although the diameters of the crystallites in nanocrystalline nanoparticles are just a few nanometers, they are polycrystalline. These variations are caused by the nanometer-sized grains' dimensionality and the many contacts between nearby crystallites [7]. Several techniques have been used to fabricate MnS thin films, including thermal vacuum evaporation [8], MBE [9], RF sputtering [10], CBD) [11], solvothermal method [12, 13] and spray pyrolysis [14] are just a few of the methods that have been used to create MnS nanoparticles. Spray pyrolysis, among other methods, is a simple and cost-effective technique that produces large-area nanoparticles without requiring complex equipment such as vacuum systems. [15, 16]. This study presents a systematic investigation of low-cost, co-precipitated Cu-doped MnS nanoparticles for DSSC photoanodes, a topic that has been rarely explored. Low-level Cu doping (1–3%) induces notable structural and optical modifications, including bandgap narrowing, resulting in nearly a twofold enhancement in DSSC efficiency compared to undoped MnS.

2. Materials and Methods

2.1 Synthesis of undoped MnS and MnS:Cu nanoparticles

Undoped MnS and MnS:Cu nanoparticles have been produced using a co-precipitation technique. To summarize, 100 ml of 0.2 M manganese nitrate was slowly mixed with 25 ml of 0.05-mole urea using a magnetic stirrer and a sonication probe for 30 minutes. Next, 10 ml of a 0.2 M Na_2S solution was added to the mixture. The solution changed to pink color. After that, the precipitate was filtered and rinsed several times with distilled water. The pink powder of MnS nanoparticles was formed. For the synthesis of MnS NPs, 25 ml of 1% and 3% copper nitrate were added to the suspension of MnS NPs (0.1 g in 20 ml D.W). After that, the precipitate was filtered, rinsed several times with distilled water, and dried for 4 hours at 110 ^{o}C. The reddish-pink powder of MnS: Cu nanoparticles was formed.

2.2 Fabrication of dye-sensitized solar cells

Initially, two pastes were prepared from the resultant powders to create sandwich-shaped DSSCs. In order to accomplish this, 0.5 g of the nano-powder was crushed in a mortar, and then 0.05 g of polyethylene glycol (PEG) was added. Distilled water, ethanol, and acetone were ultrasonically cleaned in an ultrasonic bath for 5 minutes to clean the ITO glass (80% transmission and 9 Ohm resistance). The doctor blade method was then used to apply the nano-colloid on the ITO glass substrates, and it was annealed for 30 minutes at 150°C `under nitrogen flow. The areas of the active electrodes were 2 cm². These electrodes, coated with the nano-colloid for 6 hours, were submerged in 20 mL of 1 mM N719 dye. Using a sandwich-style assembly, the DSSCs were assembled with platinum counter electrodes. Finally, the electrolyte (iodine) was introduced through small holes in the counter electrodes [17]. Sun illumination (Global AM 1.5, 100 mW/cm²) was used to test photocurrent-voltage (I–V) curves.

3. Results and Discussion

3.1 XRD Analysis

Using XRD, structural identification was performed in the 2θ range from 20° to 70°. Figure 1 depicts the XRD pattern of MnS nanoparticles formed at 110 °C. The crystallography was strong, with five main peaks corresponding to the orientations (100), (002), (101), (102), and (110), respectively. The XRD and standard ASTM data are compared to the detected peaks (JCPDS card 40-1289). The materials placed on the microscope glass slide are polycrystalline, as indicated by the sharp peaks observed. With increasing deposition doping from (1 to 3) %, the peak intensity of the (200) plane rises, suggesting that the crystallinity of the nanoparticles grows progressively. There were no diffraction peaks that corresponded to contaminants.

Using Scherrer's formula [17], the average grain size (D) is computed.

$$D = \frac{0.9\,\lambda}{\beta cos\theta} \qquad (1)$$

Where θ is the Bragg angle, β is FWHM, λ is the incoming X-ray wavelength. The low broad peak revealed that all of the nanoparticles are nano-crystalline or composed of fine grains. Table 1 presents the computed crystallite sizes for 3% Cu doping, which range from 12.60 nm to 14.37 nm for the (200) plane. The findings show that as nanoparticle doping increases, crystallite size increases as well. This behavior can be attributed to increased defects arising from the combination of Mn^{2+} and Cu^{2+} ions, since their ionic radii (0.83 and 0.87, respectively) are nearly equal. In the instance of Cu-doped MnS, there was a slight difference in the peak locations. For Cu-doped MnS, similar outcomes have been reported [18, 20].

The relation below [21] was used to compute the lattice strain (ε).

$$\varepsilon = \frac{\beta cos\theta}{4} \quad (2)$$

Where β is the FWHM, θ is the Bragg angle.

The relation below [22] was used to compute the lattice dislocation density (δ).

$$\delta = \frac{1}{D^2} \quad (3)$$

Where D is the average grain size. Figure 2 displays *D*, FWHM, strain, and dislocation of undoped MnS nanoparticles with dopant at varied concentrations of Cu. The FWHM decreases, and *D* increases due to the drop in (δ). δ and ε decrease as crystallite size rises [20]. The impact of varying doping concentrations on the MnS nanoparticles' structural parameters is summarized in Table 1. When the FWHM value of a nanoparticles is reduced (from 0.65° to 0.57°), it is noted that the crystallinity and crystallite size both improve. This can be understood because while producing the Cu-doped MnS nanoparticles, the considerably larger Mn^{2+} ions are replaced by the relatively more minor Cu^{2+} ions. This causes a drop in the lattice constants, which causes changes in the crystallite size. Similar outcomes for MnS-doped Cu have been reported. [23, 24].

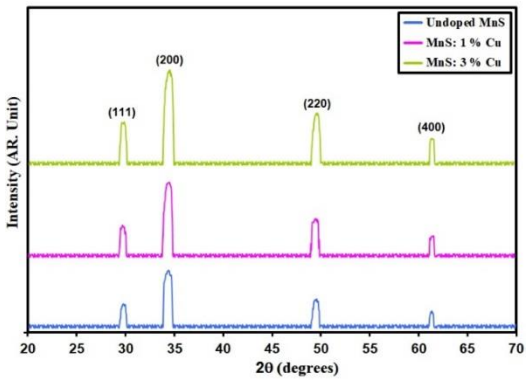

Figure 1. X-Ray diffraction patterns of grown nanoparticles

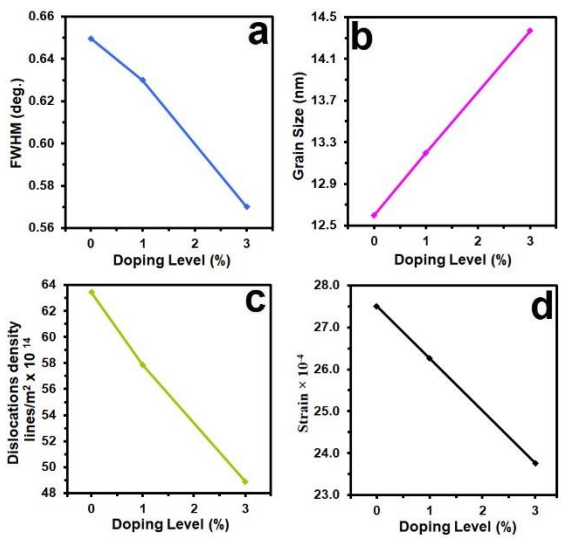

Figure 2. X-ray parameters of undoped MnS and MnS: Cu nanoparticles: (a) Full width at half maximum as a function of doping, (b) Grain size as a function of doping, (c) Dislocation density as a function of doping, and (d) Strain as a function of doping

Table 1. Microstructural parameters of undoped MnS and MnS: Cu nanoparticles

Specimen	2 θ (°)	(hkl) Plane	FWHM (°)	E_g (eV)	D (nm)	δ (× 10^{14}) (lines/m^2)	ε (× 10^{-4})
Undoped MnS	34.32	200	0.65	3.4	12.60	62.95	27.51
MnS: 1% Cu	34.30	200	0.63	3.3	13.20	57.37	26.26
MnS: 3% Cu	34.27	200	0.57	3.2	14.37	48.44	2.76

3. 2 AFM Analysis

The surface morphology was investigated using AFM. AFM instruments showed the topography of the produced Undoped and MnS: Cu nanoparticles, as illustrated in Figure 3. The surface roughness R_a of the nanoparticles is measured using 78nm x 78nm pictures. The creation of nanoparticles inside nanostructures, coupled with the particle sizes of undoped MnS and MnS doped with 1% and 3% Cu, is visible. The average particle size, Pav, ranged from 88.1 nm to 42.8 nm. With increased Cu content from 1% to 3%, the RMS surface roughness fell from 9.48 nm to 2.23 nm. Figure 3 illustrates the surface's smooth, uniform development and granular, crystalline composition with no visible flaws. This indicates that the nanoparticles' Pav decreases with increasing doping concentration. This outcome agreed with the XRD findings [25]. Table 2 displays the data of the AFM parameters.

The SEM images (Figure 4) of nanoparticles synthesized with undoped and Cu-doped MnS reveal significant morphological changes in the synthesized nanoparticles due to copper doping. Initially, the surface displays distinct, nearly flat islands. However, with increased copper doping, a noticeable transformation occurs, resulting in a more uniform surface coverage characterized by spherical nano-grains. The decrease in the size of these nano-grains with increasing copper doping concentration suggests a clear correlation between the level of copper doping and the resulting nanostructure [26, 27].

Table 2. AFM parameters of the intended nanoparticles

Samples	P_{av} (nm)	R_a (nm)	RMS (nm)
Undoped MnS	88.1	8.76	9.48
MnS: 1% Cu	49.7	5.98	8.17
MnS: 3% Cu	42.8	3.18	2.23

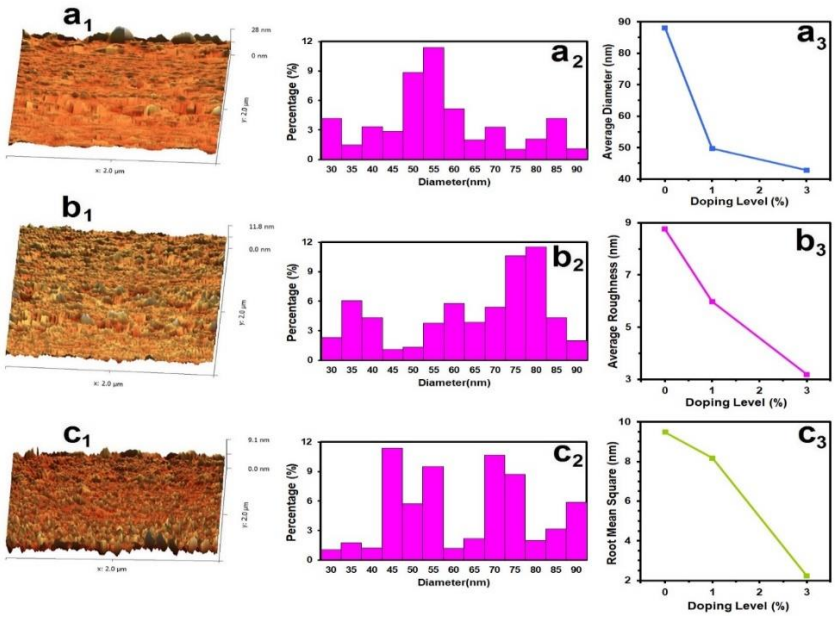

Figure 3. AFM images of the prepared films (a1, b1 and c1), granularly distributed (a2, b2 and c2) and variation of AFM parameters via doping (a3, b3 and c3)

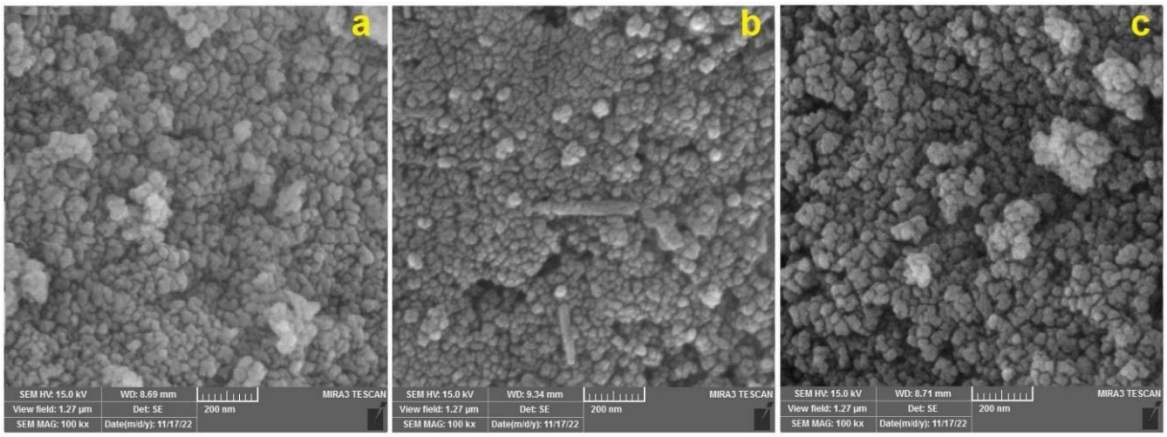

Figure 4. SEM images: (A) Undoped Cu, (B) 1% doped by Cu, and (C) 3% doped by Cu

3.3 Optical analysis

Experimental measurements are typically expressed using the percentage transmittance (T), as defined in Equation [28]:

$$T\% = \frac{I}{I_o}\% \qquad (4)$$

Where (I) denotes the light intensity after passing through the sample, (I_o) represents the initial light intensity.

Undoped MnS and MnS: Cu nanoparticles produced at various doping concentrations were studied for their transmittance (T) in the 300-900 nm region. In Figure 5, the transmittance spectra are given. The absorption edge for all the nanoparticles is about 350 nm, and we detect a considerable absorption in the UV area for all samples. All of the nanoparticles exhibit a high average T of more than 70% in the visible area. This finding is explained by the fact that, as previously demonstrated by AFM characterizations, all nanoparticles have a structure of grains with a nanoscale. Due to imperfections and porosity within the nanoparticles, T falls in the visible area as the doping concentration increases throughout the growing process. [29, 30]. Figure 6 displays the absorbance of the nanoparticles versus wavelength. It has been noted that the specimens' spectrum absorbance is relatively low between 450 and 900 nm, rapidly increases between 300 and 450 nm of the UV area, and gradually diminishes as the wavelength increases. The spectra also show that absorbance increased with increasing Cu ion concentration. [31, 32].

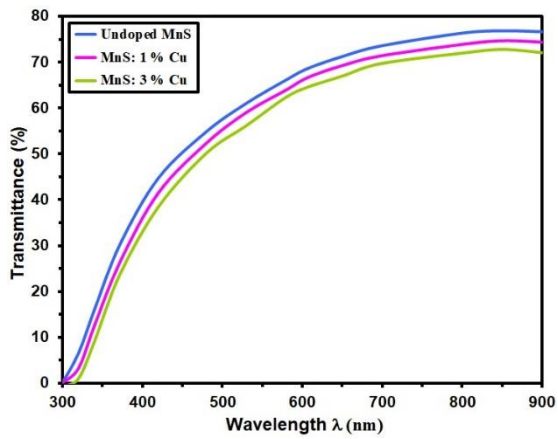

Figure **5.** Transmittance undoped Mns and MnS: Cu nanoparticles with different dopants

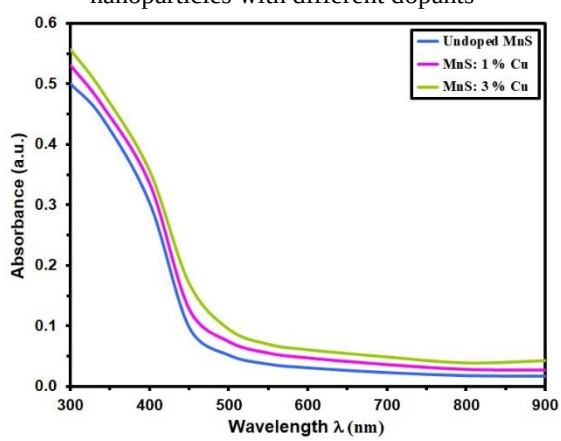

Figure **6.** Absorption of undoped MnS and MnS: Cu nanoparticles with different dopants

The optical absorption coefficient (α) is estimated via [33]:

$$\alpha = \frac{1}{d}\ln\left(\frac{1}{T}\right) \qquad (5)$$

Where (d) is the nanoparticles' thickness, and was measured to be around 200 nm, (T) is the transmittance. As observed in Figure 7, all of the nanoparticles are of high quality since every sample has a distinct absorption edge. We acknowledge that the appearance of energy states in the forbidden band at the band margins may cause the shift towards lower energies for higher doping levels. The relationship between α and incident photon energy ($h\nu$) can be illustrated as [34,35]:

$$\alpha h\nu = B(h\nu - E_g)^r \quad (6)$$

Where α is the absorption coefficient $h\nu$ photon energy, B constant, E_g is the energy gap, r = 1/2 for direct permitted transitions. The nanoparticles' plot is depicted in Figure 8 as $(\alpha h\nu)^2$ versus (hν). Undoped MnS nanoparticles have a calculated E_g of 3.4 eV. In comparison, doped MnS nanoparticles have a calculated band gap of 3.2 eV, a minor shift in Eg. This finding supports the hypothesis that as doping levels increase during growth, the optical band gap decreases. The quantum-size effect of D, which alters the nanoparticles' band gap, is attributed to the decrease in Eg with increasing Cu [36, 37].

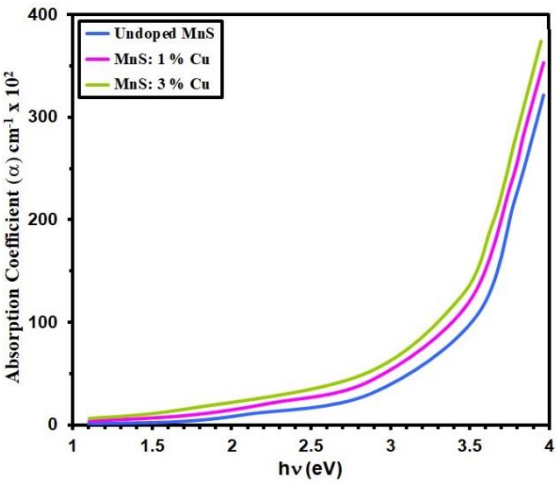

Figure 7. Absorption coefficient as a function of photon energy of undoped MnS and MnS: Cu nanoparticles with different dopants

Using the relation, the reflectance (R) data can be used to determine the refractive index (n). [38, 39]:

$$R = \frac{(n-1)^2}{(n+1)^2} \quad (7)$$

Where n is the refractive index.

This equation can be used to determine the extinction coefficient (*k*). [40, 41]:

$$k = \frac{\alpha\lambda}{4\pi} \quad (8)$$

Where λ is the wavelength. Figures 9 and 10 show the calculated (n, k) values versus wavelength. The figure shows that the refractive index (n) somewhat falls when doping concentration increases. The results demonstrate that across the spectral range from 420 nm to 500 nm, n drops from 3.18 to 3.1 before becoming practically constant with decreasing photon energy [42-44]. With increasing doping, it is discovered that *k* as a function of wavelength decreases, which may be because the dopant element alters the breadth of localized states in the optical band [45,46]. This optical absorption behavior is reflected in n and *k* behaviour.

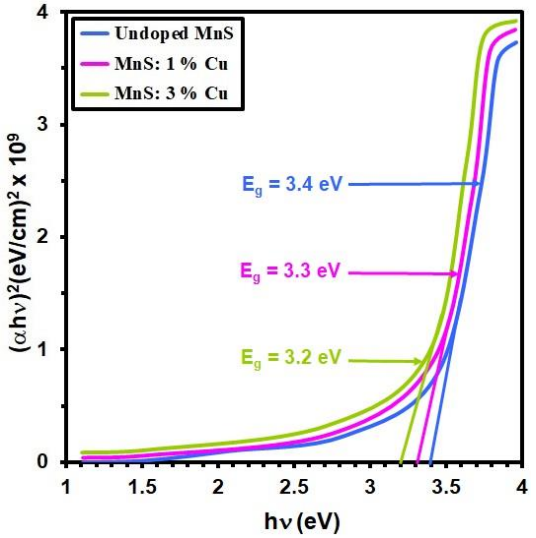

Figure 8. $(\alpha h\nu)^2$ as a function of photon energy of undoped MnS and MnS: Cu nanoparticles with different dopants

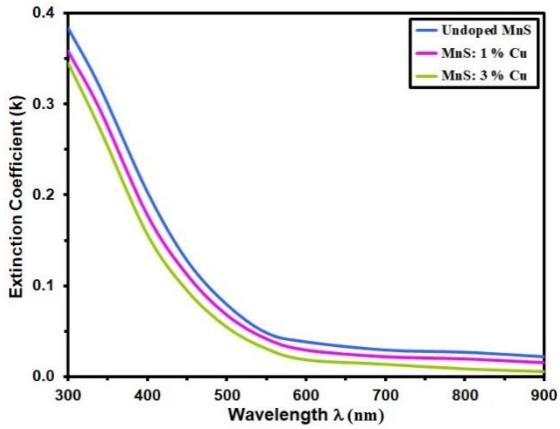

Figure 9. Extinction coefficient of undoped MnS and MnS: Cu nanoparticles with different dopants

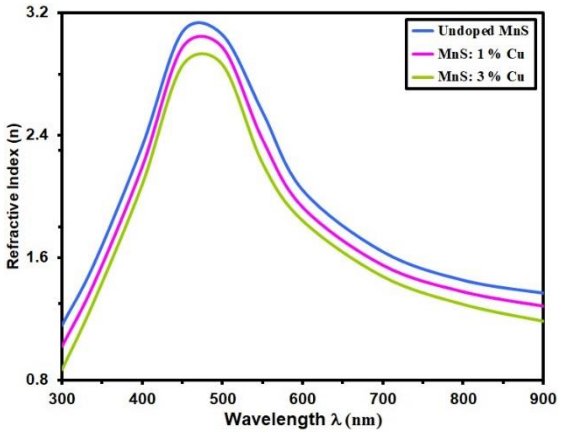

Figure 10. Refractive Index of undoped MnS and MnS: Cu nanoparticles with different dopants

3.4 J-V Characteristics

The J-V characteristics of each solar cell made up of undoped MnS and MnS:Cu nanoparticles are shown in Figure 11. Cu nanoparticles with varying doping levels. The following equations were used to calculate the fill factor and cell efficiency [47,48]:

$$\eta = \frac{pm}{pin} \times 100\% \quad (9)$$

$$F.F = \frac{Jm\ Vm}{Jsc\ V_0c} \quad (10)$$

The calculated values obtained from each solar cell's J-V curve are displayed in Table 3. The most notable trend is the change in conversion efficiency, open circuit voltage, and short-circuit current density—all correlated with the doping ratio. This may be explained by the fact that more dye is deposited on the surface as particle size increases. Consequently, a doping ratio of 3% yields the maximum short-circuit current density. This style is acceptable because the MnS nanoparticles were produced from the same MnS source and in the same manner, resulting in identical surface chemistry and particle packing. The most noticeable trend, which solely correlates with particle size, is the shift in short-circuit current density and total light conversion efficiency. While it was anticipated that smaller particles would be able to absorb more dye because of their larger surface area, it was shown that particles with lower diameters have superior dye absorption because the electrolyte diffuses more successfully through the pores, improving the light conversion efficiency as a whole. Smaller particles showed superior dye adsorption, suggesting that MnS nanoparticles of smaller particles have a more effective surface area for producing electron holes and absorbing more photons. Improving the photo electrode's ability to absorb light optically is closely linked to small particle size. According to Mie scattering theory, the small particle size works as light scattering, increasing the probability of adsorbed photons [49-51].

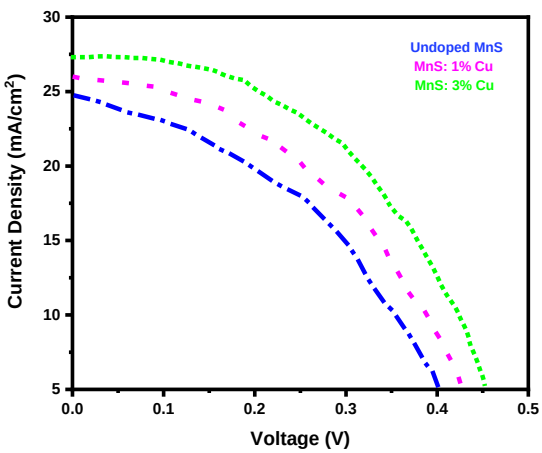

Figure 11. Current density as a function of voltage curve (J -V curves) undoped MnS and MnS:Cu nanoparticle

Table 3. DSSC parameters of the MnS and MnS:Cu nanoparticles

Photo-anode NPs	Voc (V)	J sc (A/cm^{-2})	V max (V)	J max (A/cm^{-2})	P max (W/cm^{-2})	F.F	η %

MnS	0.41	0.00242	0.26	0.00175	0.000455	0.456	0.455
MnS: 1% Cu	0.43	0.00265	0.33	0.00189	0.000624	0.548	0.624
MnS: 3% Cu	0.46	0.00277	0.39	0.00232	0.000905	0.710	0.905

4. Conclusion

This study successfully demonstrates that copper doping is a potent tool for enhancing the efficacy of MnS nanoparticles in DSSCs. The co-precipitation synthesis yielded phase-pure, nano-crystalline MnS:Cu. Critical findings reveal that Cu incorporation not only increased crystallite size but also fundamentally altered the surface morphology, resulting in a more homogeneous, finer-grained structure that is optimal for dye adsorption and light scattering. The resulting reduction in the optical band gap from 3.4 eV to 3.2 eV extended the light absorption range. These synergistic structural and optical improvements directly led to a dramatic enhancement in photovoltaic performance, with efficiency doubling from 0.455% to 0.905% in the 3% Cu-doped sample. This work conclusively establishes low-level Cu-doping as a simple and effective strategy for engineering high-performance MnS-based photoanodes for sustainable solar energy applications.

5. Imitations and Future Work

While this study demonstrates the promise of MnS:Cu nanoparticles, certain limitations exist. The power conversion efficiency, though significantly improved, remains lower than that of state-of-the-art TiO_2 -based DSSCs. The stability of the cells under prolonged illumination was not investigated. Future work will focus on optimizing the doping percentage beyond 3%, exploring core-shell structures to mitigate charge recombination, and conducting long-term stability tests. Additionally, the application of these nanoparticles in other optoelectronic devices, such as photodetectors and sensors, will be explored.

Acknowledgments

This work was supported by the College of Science at the University of Diyala, Iraq.

Nomenclature

2θ	Diffraction Angle
A	Area
α	Absorption Coefficient
B	Tauc's Relation Constant
β	Full Width at Half Maximum (FWHM)
cm	Centimeter
D	Crystallite Size
d	Thickness
δ	Dislocation Density
ε	Lattice Strain
E_g	Energy Band Gap (eV)
FF	Fill Factor
$h\nu$	Photon Energy
I	Transmitted Light Intensity
I_o	Incident Light Intensity
J	Current Density (A/m^2)
J_max	Current Density at Maximum Power (A/m^2)
J_sc	Short-Circuit Current Density(A/m^2)
k	Extinction Coefficient
λ	Wavelength (nm)
n	Refractive Index
nm	Nanometer (m)
Pmax	Maximum Power (W)
R	Reflectance (%)

References

1. Danielian, A., and Stevens, K. W. H. (1961). Exchange interactions in the polymorphic forms of MnS. Proceedings of the Physical Society, 77(1), 124–

128. https://doi.org/10.1088/0370-1328/77/1/315.

2. Hobbs, D., and Hafner, J. (1999). Magnetism and magneto-structural effects in transition-metal sulphides. Journal of Physics: Condensed Matter, 11(42), 8197–8222. https://doi.org/10.1088/0953-8984/11/42/303.
3. Kravtsova, A. N., Stekhin, I. E., Soldatov, A. V., Liu, X., and Fleet, M. E. (2004). Electronic structure of MS (M=Ca,Mg,Fe,Mn): X-ray absorption analysis. Physical Review B, 69(13), 134109. https://doi.org/10.1103/PhysRevB.69.134109.
4. Tappero, R., Darco, P., and Lichanot, A. (1997). Electronic structure of α-MnS (alabandite): An ab initio study. Chemical Physics Letters, 273(1–2), 83–90. https://doi.org/10.1016/s0009-2614(97)00591-5.
5. Viswanath, R., Naik, H. S. B., Kumar, G. S. Y., Kumar, P. N. P., Harish, K. N., and Prabhakara, M. C. (2014). Luminescence properties of blue-red emitting multilayer coated single structure ZnS/MnS/ZnS nanocomposites. Spectrochimica Acta Part A: Molecular and Biomolecular Spectroscopy, 125, 222–227. https://doi.org/10.1016/j.saa.2014.01.022.
6. Zhang, X. V., Martin, S. T., Friend, C. M., Schoonen, M. A. A., and Holland, H. D. (2004). Mineral-assisted pathways in prebiotic synthesis: Photoelectrochemical reduction of carbon(+IV) by manganese sulfide. Journal of the American Chemical Society, 126 (36), 11247–11253. https://doi.org/10.1021/ja0476415.
7. Behera, S. N., Sahu, S. N., and Nanda, K. K. (2000). Indian Journal of Physics A, 74, 81.
8. Chowdhury, M. R. I., Podder, J., and Islam, A. B. M. O. (2011). Synthesis and characterization of manganese sulfide (MnS) nanoparticles deposited by spray pyrolysis. Crystal Research and Technology, 46(3), 267–271. https://doi.org/10.1002/crat.201000511.
9. David, L., Bradford, C., Tang, X., Graham, T. C. M., Prior, K. A., and Cavenett, B. C. (2003). Growth of zinc blende MnS and MnS heterostructures by MBE using ZnS as a sulfur source. Journal of Crystal Growth, 251, 591–595. https://doi.org/10.1016/S0022-0248(02)02205-4.
10. Lee, S. M., Lee, J.-K., and Kang, Y. C. (2014). Electrochemical properties of hollow-structured MnS-carbon nanocomposite powders prepared by a one-pot spray pyrolysis process. Chemistry–An Asian Journal, 9(2), 590–595. https://doi.org/10.1002/asia.201301261.
11. Lokhande, C. D., Ennaoui, A., Patil, P. S., Giersig, M., Diesner, K., and Tributsch, H. (1998). Process and characterisation of chemical bath deposited manganese sulphide (MnS) thin films. Thin Solid Films, 330, 70–75. https://doi.org/10.1016/s0040-6090(98)00500-8.
12. Lu, J., Qi, P. F., Peng, Y. Y., Meng, Z. Y., Yang, Z. P., Yu, W. C., and Qian, Y. T. (2001). Metastable MnS crystallites through solvothermal synthesis. Chemistry of Materials, *13*(6), 2169–2172. https://doi.org/10.1021/cm010049j.
13. Mayen-Hernandez, S. A., Sandoval, S. J., Perez, R. C., Delgado, G. T., Chao, B. S., and Sandoval, O. J. (2003). Preparation and characterization of polycrystalline MnS thin films by the RF-sputtering technique above room temperature. Journal of Crystal Growth, 256, 12–19. https://doi.org/10.1016/S0022-0248(03)01315-0.
14. Mu, J., Gu, Z., Wang, L., Zhang, Z., Sun, H., and Kang, S. (2008). Phase and shape controlling of MnS nanocrystals in the solvothermal process. Journal of Nanoparticle Research,10(1), 197–201. https://doi.org/10.1007/s11051-007-9216-8.
15. Sombuthawee, C., Bonsall, S. B., and Hummel, F. A. (1978). Phase equilibria in the systems ZnS MnS, ZnS CuInS2, and MnS CuInS2. Journal of Solid State Chemistry, 25(4), 391–399. https://doi.org/10.1016/0022-4596(78)90125-1.
16. Yang, Q., Tong, X., Guo, X., Cui, Y., Zhang, Z., and Zhang, T. (2026). Nanoconfined metastable manganese sulfide in mesoporous silica enables effective suppression of microbial mercury

methylation. Water Research, 288, 124721. https://doi.org/10.1016/j.watres.2025.124721.

17. Al-Gazali, A. J., Abdulmunem, O. M., Qader, K. Y., Chiad, S. S., and Habubi, N. F. (2020). Investigation of some physical properties of Mn doped ZnS nano thin films. AIP Conference Proceedings, 2213(1), 020101. https://doi.org/10.1063/5.0000547.
18. Beltran-Huarac, J., Palomino, J., Resto, O., Wang, J., Jadwisienczak, W. M., Weiner, B. R., and Morell, G. (2014). Highly-crystalline γ-MnS nanosaws. RSC Advances, 4, 38103–38110. https://doi.org/10.1039/c4ra05561f.
19. Beltran-Huarac, J., Resto, O., Carpena-Nunez, J., Jadwisienczak, W. M., Fonseca, L. F., Weiner, B. R., and Morell, G. (2014). Single-crystal γ-MnS nanowires conformally coated with carbon. ACS Applied Materials and Interfaces, 6(2), 1180–1186. https://doi.org/10.1021/am404746k.
20. Chen, T., Tang, Y., Qiao, Y., Liu, Z., Guo, W., Song, J., Mu, S., Yu, S., Zhao, Y., and Gao, F. (2016). All-solid-state high performance asymmetric supercapacitors based on novel MnS nanocrystal and activated carbon materials. Scientific Reports, 6, 23289. https://doi.org/10.1038/srep23289.
21. Corliss, L., Elliott, N., and Hastings, J. (1956). Magnetic structures of the polymorphic forms of manganese sulfide. Physical Review, 104(4), 924–928. https://doi.org/10.1103/PhysRev.104.924.
22. Ali, R. S., Al Aaraji, N. A. H., Hadi, E. H., Abass, K. H., Habubi, N. F., and Chiad, S. S. (2020). Effect of Lithium on Structural and Optical Properties of nanostructured CuS Thin. Journal of Nanostructures, 10(4), 810–816. https://doi.org/10.22052/JNS.2020.04.015.
23. Ha, D.-H., Ly, T., Caron, J. M., Zhang, H., Fritz, K. E., and Robinson, R. D. (2015). A general method for high-performance li-ion battery electrodes from colloidal nanoparticles without the introduction of binders or conductive-carbon additives: The cases of MnS, Cu2-x S, and Ge. ACS Applied Materials and Interfaces, 7(45), 25053–25060. https://doi.org/10.1021/acsami.5b03398.
24. Jun, Y.-W., Jung, Y.-Y., and Cheon, J. (2002). Architectural control of magnetic semiconductor nanocrystals. Journal of the American Chemical Society, 124(4), 615–619. https://doi.org/10.1021/ja016887w.
25. Kan, S., Felner, I., and Banin, U. (2001). Synthesis, characterization, and magnetic properties of α-MnS nanocrystals. Israel Journal of Chemistry, 41(1), 55–61. https://doi.org/10.1560/1FB3-1PF4-72JQ-0AQC.
26. Li, Z., Ji, Y., Xie, R., Grisham, S. Y., and Peng, X. (2011). Correlation of CdS nanocrystal formation with elemental sulfur activation and its implication in synthetic development. Journal of the American Chemical Society, 133(43), 17248–17256. https://doi.org/10.1021/ja204538f.
27. Ma, C., Beckett, J. R., and Rossman, G. R. (2012). Browneite, MnS, a new sphalerite-group mineral from the Zaklodzie meteorite. American Mineralogist, 97(11-12), 2056–2059. https://doi.org/10.2138/am.2012.4336.
28. Chiad, S. S., Habubi, N. F., Abass, W. H., and Abdul-Allah, M. H. (2016). Effect of thickness on the optical and dispersion parameters of Cd0.4Se0.6 thin films. Journal of Optoelectronics and Advanced Materials, 18(9–10), 822–826.
29. Moloto, N., Moloto, M. J., Kalenga, M., Govindraju, S., and Airo, M. (2014). Synthesis and characterization of MnS and MnSe nanoparticles: Morphology, optical and magnetic properties. Optical Materials, 36(1), 31–35. https://doi.org/10.1016/j.optmat.2013.06.023.
30. Peng, L., Shen, S., Zhang, Y., Xu, H., and Wang, Q. (2012). Controllable synthesis of MnS nanocrystals from a single-source precursor. Journal of Colloid and Interface Science, 377(1), 13–17. https://doi.org/10.1016/j.jcis.2012.03.052.
31. Pradhan, N., Katz, B., and Efrima, S. (2003). Synthesis of high-quality metal sulfide nanoparticles from alkyl xanthate single precursors in alkylamine solvents. The Journal of Physical Chemistry

B, 107(51), 13843–13854. https://doi.org/10.1021/jp0364525.

32. Tang, Y., Chen, T., and Yu, S. (2015). Morphology controlled synthesis of monodispersed manganese sulfide nanocrystals and their primary application in supercapacitors with high performances. Chemical Communications, 51(43), 9018–9021. https://doi.org/10.1039/c5cc01700a.
33. Thomson, J. W., Nagashima, K., Macdonald, P. M., and Ozin, G. A. (2011). From sulfur-amine solutions to metal sulfide nanocrystals: Peering into the oleylamine-sulfur black box. Journal of the American Chemical Society, 133(13), 5036–5041. https://doi.org/10.1021/ja1109997.
34. Tian, L., Yep, L. Y., Ong, T. T., Yi, J., Ding, J., and Vittal, J. J. (2009). Synthesis of NiS and MnS nanocrystals from the molecular precursors (TMEDA)M(SC{O}C6H5)2 (M = Ni, Mn). Crystal Growth and Design, 9(1), 352–357. https://doi.org/10.1021/cg800536w.
35. Hassan, E. S., Elttayef, A. K., Mostafa, S. H., Salim, M. H., and Chiad, S. S. (2019). Silver oxides nanoparticle in gas sensors applications. Journal of Materials Science: Materials in Electronics, 30(17), 15943–15951. https://doi.org/10.1007/s10854-019-01679-1.
36. McNaughter, P. D., Moore, J., Yeates, S. G., and Lewis, D. J. (2024). Semiconductor deposition via laser printing of a bespoke toner containing metal xanthate complexes. ACS Applied Engineering Materials, 2(5), 1225–1233. https://doi.org/10.1021/acsaenm.3c00709.
37. Chen, C.-K., Chen, B.-H., and Huang, M. H. (2023). Low-temperature growth of rock salt MnS nanocrystals with facet-dependent behaviors. Chemistry of Materials, 35(18), 7859–7866. https://doi.org/10.1021/acs.chemmater.3c01883.
38. Chaudhary, K., Shahid, M., Zulfiqar, S., Alzahrani, F. M. A., Al-Buriahi, M. S., Warsi, M. F., and Cochran, E. W. (2023). Hydrothermal self-assembly of α-MnSe-loaded honeycomb-like biomimetic Ti3C2Tx/graphene aerogel microstructure (α-MnSe/Ti3C2Tx/rGO) as efficient electrode material for energy storage application. Energy and Fuels, 37(17), 13435–13448. https://doi.org/10.1021/acs.energyfuels.3c01882.
39. Hussin, H. A., Al-Hasnawy, R. S., Jasim, R. I., Habubi, N. F., and Chiad, S. S. (2020). Optical and structural properties of nanostructured CuO thin films doped by Mn. Journal of Green Engineering, 10(9), 7018–7028.
40. Yassin, G., Pönitz, E., Huittinen, N. M., Schild, D., Konheiser, J., Müller, K., and Barkleit, A. (2025). Phase characterization of (MnS) inclusions and Mo precipitates in reactor pressure vessel steel from Greifswald nuclear power plant. Journal of Nuclear Engineering, 6(2), 12. https://doi.org/10.3390/jne6020012.
41. Muhammad, S. K., Hassan, E. S., Qader, K. Y., Abass, K. H., Chiad, S. S., and Habubi, N. F. (2020). Effect of vanadium on structure and morphology of SnO2 thin films. Nano Biomedicine and Engineering, 12(1), 67–74. https://doi.org/10.5101/nbe.v12i1.p67-74.
42. Jancalek, J., Kurka, M., Rodriguez-Pereira, J., Slang, S., and Krbal, M. (2025). Nanostructured MnS-based thin films deposited from propylamine solutions of elemental sulfur and manganese. Materials Advances, 6(20), 7599–7608. https://doi.org/10.1039/D5MA00519A.
43. Fakhri-Mirzanagh, S., Shojaei, S. H. R., Pirgholi-Givi, G. R., and Azizian-Kalandaragh, Y. (2025). Efficient photodegradation of methylene blue by CdS-based nanocomposites. Journal of Materials Science: Materials in Electronics, 36(14). https://doi.org/10.1007/s10854-025-14854-4.
44. Barry, L., Copley, M., Holmes, J. D., Otway, D. J., Kazakova, O., and Morris, M. A. (2007). Synthesis and characterization of nanoparticulate MnS within the pores of mesoporous silica. Journal of Solid State Chemistry, 180(12), 3443–3449. https://doi.org/10.1016/j.jssc.2007.10.004.
45. Meng, J., Zhao, Y., Li, Z., Wang, L., and Tian, Y. (2016). Phase transfer preparation

of ultrasmall MnS nanocrystals with a high performance MRI contrast agent. RSC Advances, 6(8), 6878–6887. https://doi.org/10.1039/c5ra24775f.

46. Lacey, H. R., Dobson, K. D., and Hernández-Pagán, E. A. (2025). Flexible cation exchange environment via ligand-free metal chalcogenide thin films. ACS Nanoscience Au, 5(1), 9–20. https://doi.org/10.1021/acsnanoscienceau.4c00023.
47. Eriksson, L., and Kalinowski, M. P. (2001). Mn1-x Fex S, x ≅ 0.05, an example of an anti-wurtzite structure. Acta Crystallographica Section E: Structure Reports Online, 57(10), i92–i93. https://doi.org/10.1107/S1600536801015714.
48. Zhou, J., Huang, F., Xu, J., and Wang, Y. (2013). Cu1.94S-MnS dimeric nanoheterostructures with bifunctions: Localized surface plasmon resonance and magnetism. CrystEngComm, 15(49), 4217–4220. https://doi.org/10.1039/c3ce00015j
49. Kim, D. S., Lee, J. Y., Na, C. W., Yoon, S. W., Kim, S. Y., Park, J., Jo, Y., and Jung, M. H. (2006). Synthesis and photoluminescence of Cd-doped α-MnS nanowires. The Journal of Physical Chemistry B, 110(37), 18262–18266. https://doi.org/10.1021/jp063965z.
50. Ge, J. P., and Li, Y. D. (2003). Controllable CVD route to CoS and MnS single-crystal nanowires. Chemical Communications, (20), 2498–2499. https://doi.org/10.1039/b307452h.
51. Ge, J. P., Wang, J., Zhang, H. X., and Li, Y. D. (2004). A general atmospheric pressure chemical vapor deposition synthesis and crystallographic study of transition-metal sulfide onedimensional nanostructures. Chemistry–A European Journal, 10(14), 3525–3530. https://doi.org/10.1002/chem.200305762.